Original Research

Optical, and Electronic Properties of Ni-Doped $BiFeO_3$ Nanoparticles

Sake Devendra [1,2], L. Siva Sankara Reddy [1,*], M. Chandrasekhar [3], D. Baba Basha [4,*]

[1] Department of Physics, Sri Krishnadevaraya University, Anantapuramu 515003, India;
[2] Department of Physics, Government College (A), Ananthapur 515001, India;
[3] Department of Physics, Chaitanya Bharathi Institute of Technology, Hyderabad 500075, India;
[4] Department of Information Systems, College of Computer and Information Sciences, Majmaah University, Al'Majmaah 11952, Saudi Arabia
* Correspondence: Siva Sankara Reddy, reddy.lss@gmail.com; D. Baba Basha, b.dudekula@mu.edu.sa

Received: 18th November, 2025; Accepted: 28th January, 2026

Abstract: $Bi_{1-x}Ni_xFeO_3$ (x = 0.20–0.80) nanoparticles were prepared using the hydrothermal method. Rhombohedral structure along with few secondary phases are confirmed from obtained X-ray diffraction (XRD) patterns. The microstructure confirmed structures similar to nanospheres and small nanorods. An agglomeration is noticed among the nanoparticles of x = 0.2–0.8 owing to magnetic interactions. The Tauc's plots are drawn to evaluate the optical bandgap (E_g) as a function of Ni-content. The dielectric constant, and loss parameters were studied as a function of Ni-content and frequency. In addition, the dielectric modulus formalism was discussed to evaluate the space charge effect and charge carrier behavior. The Nyquist plots were drawn and noted to be incomplete relaxation for all the samples.

Keywords: perovskite; microstructure; nanoparticles; optical; electronic

1. Introduction

Perovskite materials received much attention in science and technology due to their peculiar properties like dielectric, ferroelectric, photocatalytic, nanocatalytic, piezoelectric, pyroelectric, etc., [1]. All these properties led the perovskites to achieve the applications in the charge stored capacitors, ferroelectric memory devices, piezo-sensors, solar cells (SCs)/photovoltaic devices, optoelectronic devices, and so on [2]. It is a familiar fact that the perovskite reveals an ABO_3 chemical structure, wherein, the 'A' corresponds to divalent/trivalent elements, and the 'B' refers to the trivalent/tetravalent element [3]. Further, it is also noticed that some of the perovskites exhibited magnetic, dielectric, ferroelectric, and ferroelastic nature. Such systems are considered as multiferroic perovskites [4]. Among these multiferroics, the well familiar system is $BiFeO_3$ [BF]. It showed good attention due to the applications such as spintronics, memory, energy storage, energy conversion, sensors, actuators, medical (like CT scan), catalysis, photonic devices, optoelectronics, tunnel junctions, etc., [4–6]. The perovskite-based materials, 2D perovskites, double perovskites, graphene-based perovskites, graphitic carbon nitride, etc., have also shown much attention towards the above-mentioned applications [6]. A significant research work is done on bismuth ferrite materials for several applications. In this regard, Verma et al. [7], synthesized the BF nanosystem, and reported the magnetoelectric nature of the samples. Visakh et al. [8], addressed the synthesis, and various characterizations of multiferroic nanocomposites revealing several applications. Celis et al. [9], introduced different mechanisms in order to control the multiferroic properties of BF nanoparticles. Indriyani et al. [10], fabricated the BF nanoparticles via one-pot method through abelmoschus esculentus leaves, and showed the photocatal ytic dye degradation activity [11].

Amdouni et al. [12], prepared the BF nanoparticles, and investigated the piezo-photocatalytic activity. Parvathy et al. [12], explicitly reported the atomic scale insights on the growth of BF nanoparticles. Parida et al. [13], prepared the BF nanoparticles via the plant extraction approach, and reported the photocatalyst degradation of MB (methylene blue) dye application. Basith et al. [14], synthesized the BF nanoparticles at low operating temperatures, and confirmed the high magnetization, photocatalytic dye degradation, and hydrogen evolution. Bai et al. [15], introduced various approaches for growing the BF crystals. Cheng et al. [16], developed the BF nanoparticles, and suggested for the selective n-butanol gas sensing applications by creating the abundant oxygen vacancies. Wu et al. [17], synthesized the BF nanoparticles, and reported the progress of photocatalytic activity via the electrical polarization. Wu et al. [18], prepared the BF nanoparticles which are of strong pyro-catalysis in nature under a room temperature cold hot alternation. Mocherla et al. [19], reported bandgap which was tunable in BF nanoparticles, and explained the role of microstrain, and defects. Prince et al. [20], developed the tuning of a few properties of BF such as structure, optical, and magnetism via the annealing. Masoudpanah et al. [21], synthesized the BF nanoparticles, and illustrated the structure, magnetic nature, and photocatalytic activity.

Besides, doping is performed extensively on BF nanoparticles for different applications. In view of this, Othman et al. [22], synthesized, and studied the structure, magnetic, and electric properties of Co-doped BF nanoparticles. Haider et al. [23] prepared $BiCoFeO_3$ nanoparticles pertaining to the high concentration of Co and presented their electrical and magnetic properties. Poulos et al. [24], addressed the effect of Sm, and Co dopants on the physical properties of BF nanoparticles including the control mechanisms. Shrimali et al. [25] studied the influence of magnetic field on dielectric properties of Co substituted BF nanoparticles and confirmed the magnetoelectric nature of samples. Gu et al. [26], developed the $BiCoSmEuFeO_3$ nanoparticles, and determined the super-absorption capacity, and electrochemical oxygen evolution. Apostolova et al. [27] investigated magnetoelectric coupling effects for $BiTbFeO_3$ nanoparticles. Gu et al. [28], fabricated $BiSmFeO_3$ particles and evidenced magnetic nature by studying the magnetic properties. Also, the optical properties are investigated around the morphotropic phase boundary. Haruna et al. [29], demonstrated the photocatalytic activity in organic dyes by introducing various dopants into the BF system. Wang et al. [30], studied various properties by doping the nickel element into the BF system. Mishra et al. [31], clearly explained the photoluminescent activity including the energy levels of $BiNiFeO_3$. Nadeem et al. [32,33], synthesized the Ni-doped BF nanoparticles, and reported the enhancement of photocatalytic performance, and temperature dependent dielectric behavior. Cantera et al. [34], explicitly observed the structural transformation in the XRD analysis, and reported the ferroelectric, dielectric, and ferromagnetic nature of the $BiNiFeO_3$. Banu et al. [35], developed the $BiNdNiFeO_3$ nanoparticles, and suggested for spintronic applications thereby showing the dopant effect. Sarkar et al. [36], offered a clear picture on the differences between the undoped, and Ni-doped BF nanoparticles (prepared via solution combustion route) in terms of structure, electronic behavior, and magnetic nature. Mukherjee et al. [37], developed the $BiNiCoFeO_3$ nanoparticles via chemical route, and reported the effect of the cations on different multiferroic properties of the BF system. Ponraj et al. [38], ensured the photocatalytic degradation of acid red-85 dye in the case of Ni-doped BF nanoparticles. Preethi et al. [39], illustrated in detail about the doping effect in the case of BF bulk, and nanoparticles on various properties such as structural, dielectric, electrical, magnetic, ferroelectric, ferromagnetic, ferroelastic etc. Routray et al. [40] studied the impact of gamma rays on electronic, magnetic, structure, ferroelectric properties and transformations among these properties.

This detailed literature survey ensured that the research work is done on Ni-doped BF nanoparticles. But the methodology is different for different samples. That is, it manifests that the solution and alloying techniques like chemical route, combustion method, sol-gel, ball milling etc., are used to synthesize the samples. But the hydrothermal method was not opted, which is considered as a technique that brings lots of changes in microstructure and further inducing the changes in other dependent properties. Moreover, the properties were not studied collectively in a single literature paper providing the difference and connectivity of all properties. Therefore, in the current work, authors focused on synthesizing $Bi_{1-x}Ni_xFeO_3$ (x = 0.20–0.80) (BNFO) nanoparticles using

hydrothermal method. The synthesis method reveals several advantages in general like low operating temperatures (100 °C–150 °C), inexpensive, usage of low-cost nitrates as compared to oxides, high homogeneity, good crystallinity, less time consuming etc. Upon preparing the BNFO nanoparticles, the samples are intended to investigate the structure, morphology, nanoparticle confirmation, optical bandgap, functional groups/metal oxide bonds, dielectric behavior, etc.

2. Synthesis method and characterization

At the outset, for the synthesis of $Bi_{1-x}Ni_xFeO_3$ nanoparticles (x = 0.2–0.8), initial precursor materials such as [$Bi(NO_3)_3.5H_2O$, ≥ 99.99% purity, Sigma-Aldrich], Nickel (II) nitrate hexahydrate [$Ni(NO_3)_2.6H_2O$, 99.92% purity, Sigma-Aldrich], and Iron (III) nitrate nonahydrate [$Fe(NO_3)_3.9H_2O$, 99.99% purity, Sigma-Aldrich, USA] were considered. In addition, the NaOH pellets were taken which acts as the mineralizer, stabilizing the pH, facilitator for dissolving the materials, precipitation of reactants etc., during the BNFO crystal growth process. As a whole, the reaction kinetics will be influenced by NaOH solution. The preparation of BNFO nanoparticles is similar to the method provided in the literature [41,42]. A stepwise procedure for the synthesis is depicted in Figure 1. The precursors were first dissolved and stirred for 2 h to obtain a delicious BNFO solution. The NaOH solution was poured into it during the stirring process. Therefore, the reactive atmosphere among the participants gets developed in the BNFO solution. From this solution BNFO nanoparticles were prepared using autoclave process and centrifuged to remove the water content. After the centrifugation process, the remaining sample is heated at 50 °C for 2 h to expel the moisture from the nanoparticles. The powder obtained in such a way was grinded well using agate mortars and made into pellets using hydraulic press by applying the pressure ranging from 2 tons. The resultant powder, and pellets are characterized using the X-ray diffractometer (Bruker XRD, wavelength of $Cu_{K\alpha}$ = 0.15406 nm), Field-emission scanning electron microscopy (Ultra 55 FE-SEM, Carl Zeiss), Transmission electron microscopy (TEM, Model JEOL JEM 2100), UV-Visible spectrophotometer (JASCO, V-670 PC), FT-IR spectrophotometer (IR affinity-1, Shimadzu), LCR controller (HIOKI 3532-50) for studying the structure, microstructure, bandgap analysis, metal oxide bonds, dielectric, conductivity, impedance, etc., of BNFO nanoparticles.

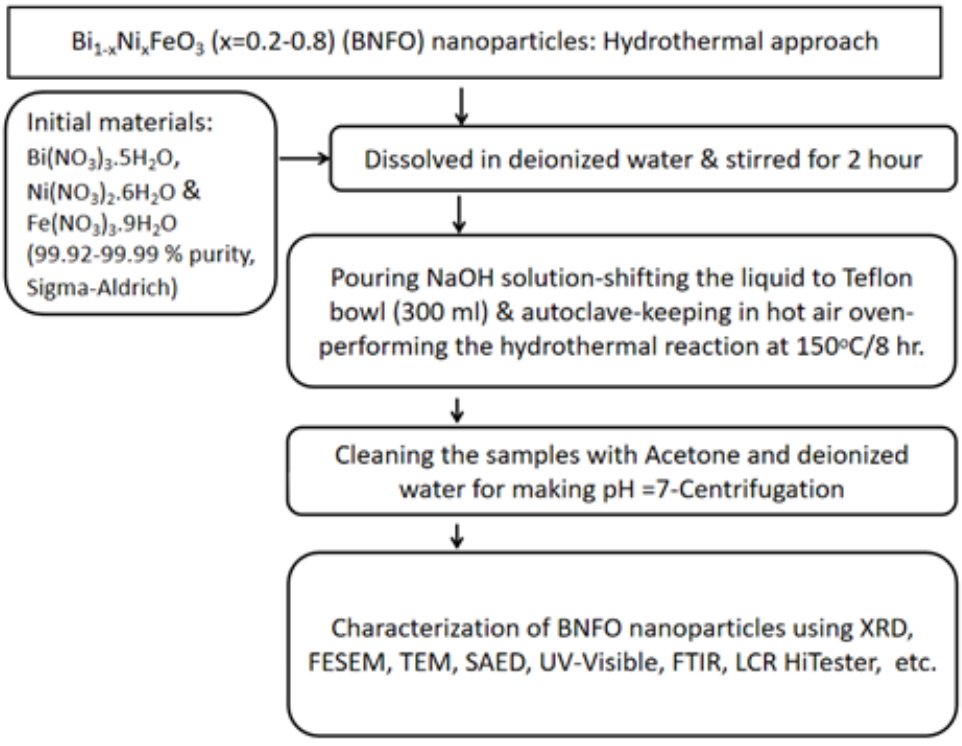

Figure 1. Process involved in synthesis of $Bi_{1-x}Ni_xFeO_3$ (x = 0.20–0.80) nanoparticles.

3. Result and discussion

Figure 2 shows XRD patterns of BNFO nanoparticles. These samples with x = 0.20, 0.60 and 0.80 show high crystallinity pertaining to (104), and (110) reflection planes. The x = 0.4 reveals the same consisting of the low intensity. Herein, the XRD patterns, the intensity is depending on the number of crystallites undergoing diffraction when compared to the $Cu_{K\alpha}$ wavelength. These crystallites are smaller in number in the case of x = 0.4 while they are at larger extent for the rest of the samples. The maximum intense peak is expressing the slit behavior. It is the most common nature of compounds wherein; the trivalent element is present in the system. Owing to the presence of trivalent element, the microstrain gets developed leading to the peak splitting behavior pertaining to the second reflection plane. Similar observations are noticed in literature [43]. According to Shannon Ionic radii information [44], it is confirmed that cations involved in BNFO system have an ionic radius of 0.096 nm [Bi^{3+}], 0.072 nm [Ni^{2+}], 0.064 [Fe^{3+}] nm and 0.063 nm [Fe^{2+}]. It is evident from this data that upon doping the Ni into the perovskite BF system, the Ni^{2+} cations cannot occupy the Bi position due to two factors. One is the huge ionic radii difference (25% variation) which can develop the fluctuation of the site having unstable structure (the less tolerance factor), and the other one is, valency mismatch (+3 and +2). Therefore, the probable occupancy goes to ferric ions (Fe^{3+}). The reason is that the ionic radii of ferric, and nickel cations are having small variation, and hence, the chances are very high to occupy the ferric ion site with the nickel ions. However, the occupancy can expand the lattice site's dimensions which increases lattice constants and unit cell volume.

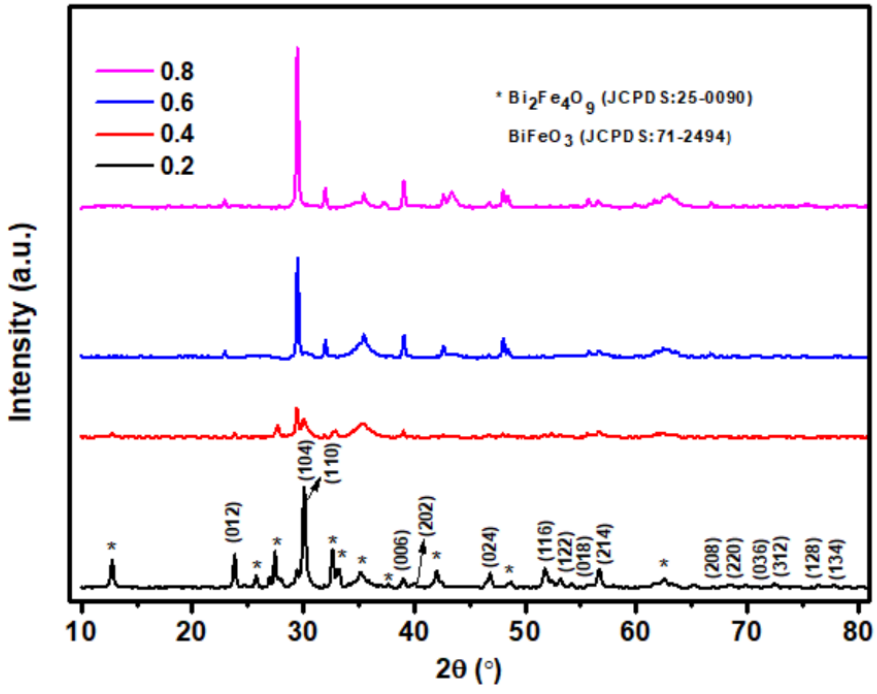

Figure 2. XRD patterns of $Bi_{1-x}Ni_xFeO_3$ (x = 0.20–0.80) nanoparticles.

Practically, it is seen in Table 1. The lattice parameters demonstrate that the BNFO structure is rhombohedral (trigonal) including few secondary phases of $Bi_2Fe_4O_9$ (indexed by * symbol) (JCPDS file No. 25-0090). The formation of a secondary phase is a common phenomenon in the case of multiferroic perovskites pertaining to the trivalent element as one of the elements as reported by

Nadeem et al. [32]. The primary phases are on par with the BF reflection planes as indicated in JCPDS file No. 71-2494. The lattice constants and unit cell volume parameters of BNFO nanoparticles are determined using unit cell software and shown in Table 1. The values increased from 5.571 to 5.581 Å (a = b) and 13.875–13.882 Å (c) with respect to Ni-content. 'V' is found to be increasing in a minute manner ranging from 372.92 to 374.45 $Å^3$. The crystallite size value '*D*' is calculated using Scherrer equation [45]. The crystallite size is found for individual peaks, and at the end the average value is taken and shown in Table 1. These results indicated the non-consistent *D*-values (45.5, 58.2, 52.9 and 69.1 nm). However, it reveals the inversely proportional relationship with change in FWHM, (or strain β: 0.781, 0.686, 0.720 and 0.485) with increase in 'x'. The X-ray density for x = 0.20–0.80 is carried out using the equation $\rho_x = (Z*CMW)/(N*V)$, in which Z is the net atoms per unit cell for trigonal structure, CMW refers to compositional molecular weight and 'N' the Avogadro's number. The value decreased from 8.9 to 5.7 g/c.c., with respect to 'x'. This can be ascertained by the decreasing trend of compositional molecular weight from 250.77 to 160.60 drastically. The relationship variation implied a fact that the huge decrement is seen at high concentration of Ni. The surface area ($S = 6000/(\rho_x*D)$) of nanoparticles is usually high, and noticed a decreasing trend from x = 0.20–0.80 with a change from 33.6 to 13.1 m^2/g. The trend of the obtained results almost follows the similar trend as reported in the literature [46–48].

The microstructure is examined via the FESEM, and TEM images as shown in Figures 3 and 4. The FESEM of x = 0.20–0.80 reveals high homogeneity, well defined nanosized grains (almost), and few small sharp structures inside the morphology. The increasing Ni-content addressed the evolution of some flat fiber kind of structures which occur owing to the presence of trivalent cation. The presence of trivalent ions can induce vibrations among the grains and further leads to the development of the nucleation process as mentioned in the literature [49]. Afterwards, linear intercept method is used to deduce mean grain size (G_a) [46]. In this method, the test lines (6 in this work) are drawn for the FESEM image of each sample and counting of grains that intersect with the test line is done. After this, values are substituted in the equation to get grain size. Grain size is averaged for all test lines and displayed in Table 1. Results indicated that the variation is not monotonic, but a similar trend is found in the crystallite size as a function of Ni-content. As result, the values are identified to be altering between 129.3 and 186.8 nm. Anyhow, this kind of manner can be usually attributed to the strain formed during the reaction process to form final compounds. The TEM images, and electron diffraction patterns of BNFO nanoparticles illustrated the clustered like nanoparticles demonstrating the existence of magnetic interaction among them. In general, the multiferroic nanoparticles contain the magnetic interactions which can happen normally due to the agglomeration of nanoparticles. Few of the flat nanostructures are seen even in TEM images which resemble the FESEM analysis. The selected area electron diffraction patterns (SAED) show the concentric circular rings having high intensity for almost all samples. The samples for x = 0.20, 0.60 and 0.80 offered high intensity of the electron diffraction patterns while x = 0.40 has little low intensity which is already reflected in the XRD patterns. This implies that there is a good agreement between different characterizations supporting the results obtained.

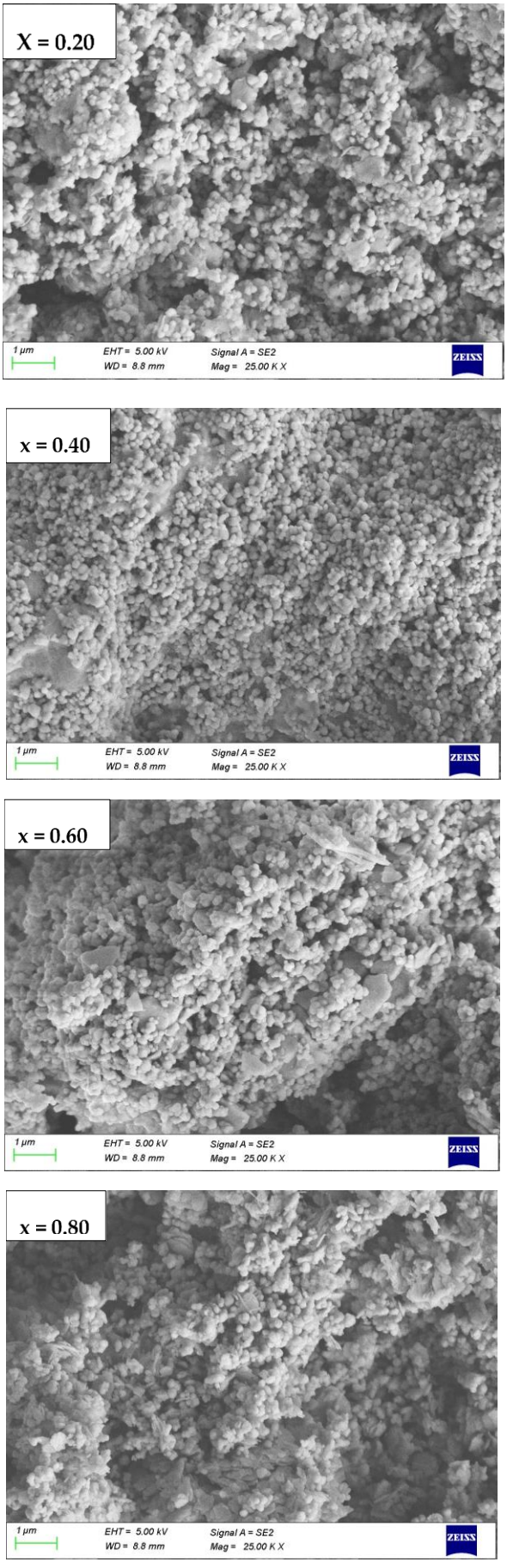

Figure 3. FESEM images of $Bi_{1-x}Ni_xFeO_3$ (x = 0.20–0.80) nanoparticles.

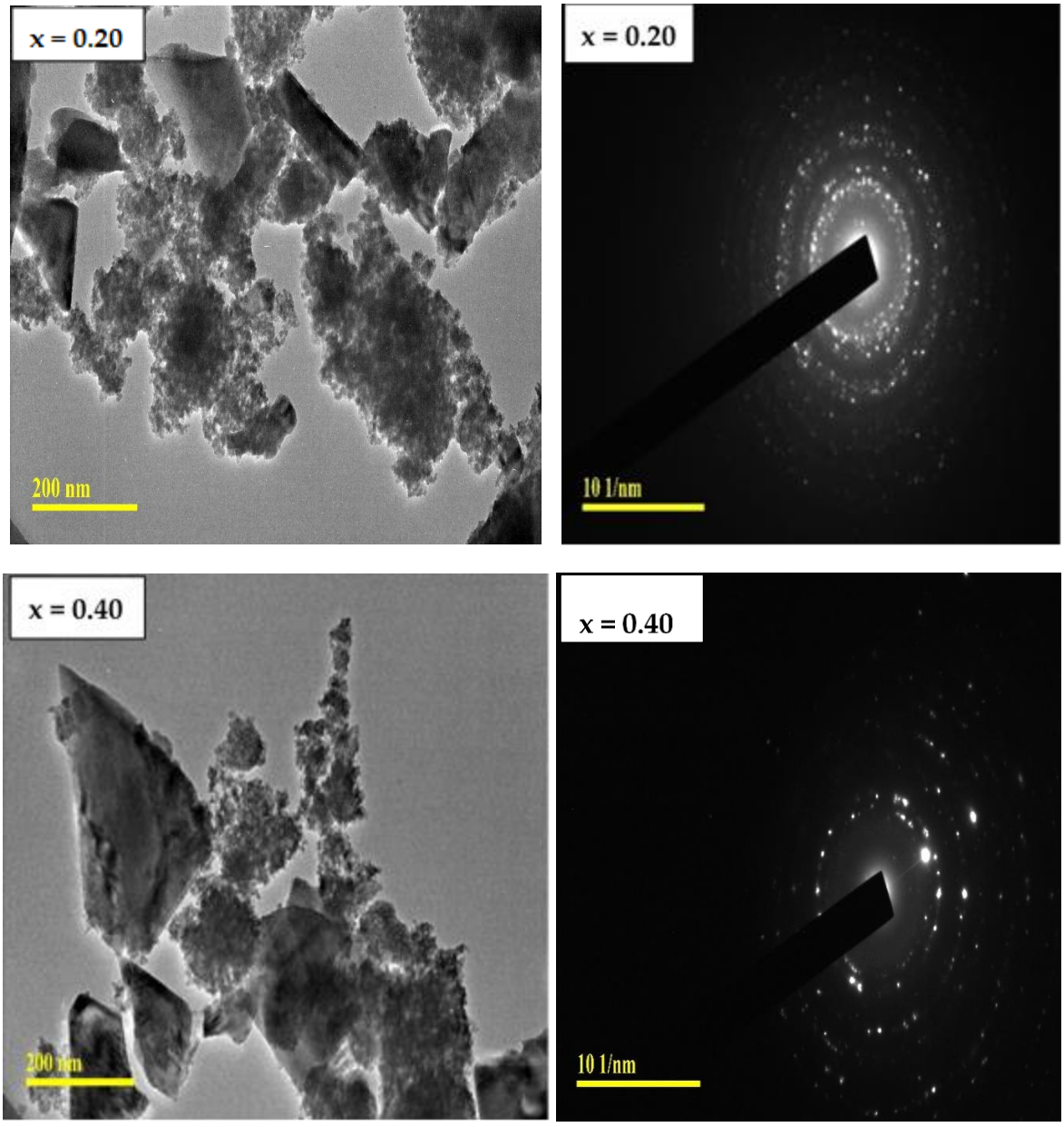
x = 0.20
200 nm
x = 0.20
10 1/nm
x = 0.40
200 nm
x = 0.40
10 1/nm

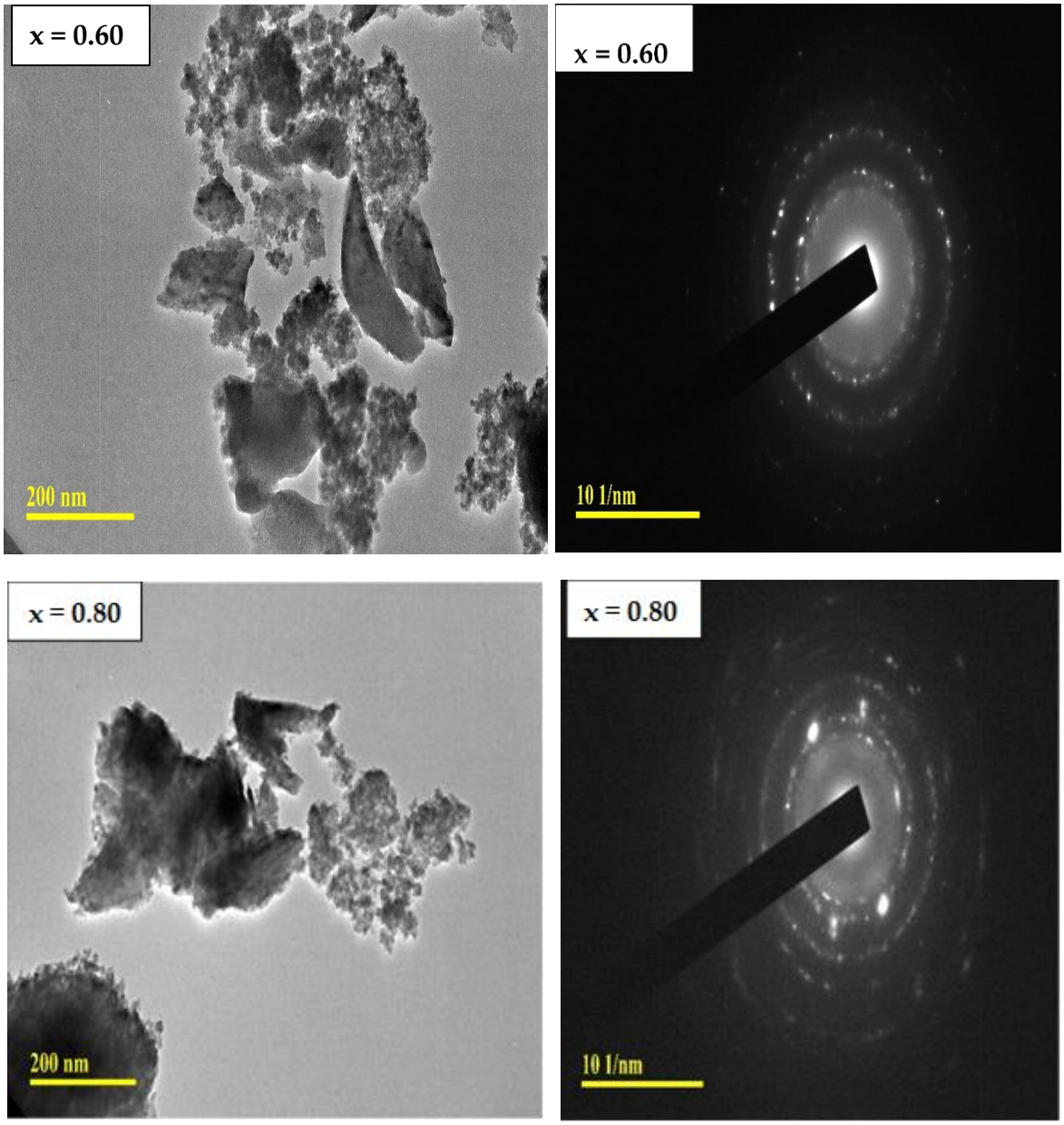

Figure 4. TEM and SAED patterns of $Bi_{1-x}Ni_xFeO_3$ (x = 0.20–0.80) nanoparticles.

4. Materials and methods

Materials and methods should be described with sufficient details to allow others to replicate and build on published results. Please note that publication of your manuscript implicates that you must make all materials, data, computer code, and protocols associated with the publication available to readers. Please disclose at the submission stage any restrictions on the availability of materials or information. New methods and protocols should be described in detail while well-established methods can be briefly described and appropriately cited.

Research manuscripts reporting large datasets that are deposited in a publicly available database should specify where the data have been deposited and provide the relevant accession numbers. If the accession numbers have not yet been obtained at the time of submission, please state that they will be provided during review. They must be provided prior to publication.

Interventionary studies involving animals or humans, and other studies require ethical approval must list the authority that provided approval and the corresponding ethical approval code.

Table 1. Structural and physical parameters of BNFO nanoparticles.

x	0.20	0.40	0.60	0.80
D (nm)	45.5 ± 0.624	58.2 ± 0.841	52.9 ± 0.794	69.1 ± 0.386
a = b (Å)	5.571	5.576	5.579	5.581
c (Å)	13.875	13.878	13.880	13.882
FWHM (β)	0.781	0.686	0.720	0.485
V (Å3)	372.92	373.67	374.13	374.45
CMW (g/mole)	250.77	220.71	190.65	160.60
ϱt (g/c.c.)	8.932	7.845	6.769	5.697
S (m2/g)	33.60	19.10	14.80	13.10
Eg (eV)	2.928	2.541	2.334	2.723
Ga (nm)	130.8	186.8	129.3	138.3

The function of reflectance ($F(r) = 0.5(1-r)^2/r$, r = reflectance) or Kubelka-Munk function is calculated for the data received from UV-Visible spectral studies of BNFO samples. The absorption coefficient (α) is calculated by considering the direct proportional relationship with the function of reflectance. Therefore, the F(r) is taken as α, and furthermore, the Tauc's plots are drawn as shown in Figure 5. The plots are drawn between hυ versus $(\alpha h\upsilon)^2$ using the equation: $(\alpha h\upsilon)^n = m((h\upsilon - E_g)$. In case of direct transition, exponent n equals to 2 while the direct forbidden reveals n = 2/3, and the indirect transitions express n = 1/2 [46–48]. In case of BNFO, the *n*-value for direct transition is considered. In the Tauc's plots, it is seen that the linear portion is extrapolated towards the hυ-axis. The intersecting point of the axis demonstrates the E_g value. As per the obtained results 'E_g' for x = 0.20–0.60 decreased from 2.928–2.334 eV while for x = 0.8, it increased to 2.723 eV. The BNFO samples are of nano in nature pertaining to the larger number of defects/oxygen vacancies. These can trap the electrons, and therefore, the delocalization of electrons takes place. With increase in Ni-content, the delocalization of electrons seemed to have increased leading to the decrease of bandgap from x = 0.20 to x = 0.60 while increased for x = 0.80, owing to decrease in oxygen vacancies [46]. The FTIR spectra of BNFO nanoparticles are recorded as shown on Figure 6. The spectra of x = 0.20–0.80 shows the formation of several absorption bands (Table 2). For x = 0.20, 0.40, 0.60 and 0.80 bands/peaks are shown at 769.23, 1055.3, 1380.6, 1651.4 and 3595.3 cm^{-1}, 706.7, 1063.3, 1380.6, 1435.1, 1473.5, 1620.9 and 3440.71 cm^{-1}, 815.7, 1055.3, 1372.6, 1481.6, 1636.2 and 3595.4 cm^{-1}, and 691.5, 1070.5, 1388.6, 1411.9, 1488.7, 1628.2 and 3424.7 cm^{-1}, respectively. The bands formed around 400–500 cm^{-1} are the indication for the formation of metal oxide bonds like Bi-O, Ni-O and Fe-O. The bands varying between 691.5 and 815.7 cm^{-1} can be attributed to the formation of secondary phase structures in the BNFO perovskite system. Similar kind of observation is found in the literature elucidating the secondary phase structure from the FTIR spectral study [50–56]. Likewise, the peaks formed between 1055.3 and 1070.5 cm^{-1} are also an indication for the secondary phase structure [50]. The formed bands between the wavenumbers 1372.6–1388.6 cm^{-1} and 1411.9–1488.7 cm^{-1}, are associated with O-H bond bending vibrations that arise from atmospheric OH-absorption of BNFO

nanoparticles [50]. Further, the peaks developed at the range of 1620.9–1651.4 cm^{-1} and 3424.7–3595.4 cm^{-1} are due to O-H stretching and bending vibrations of H_2O molecules absorbed by the samples [50].

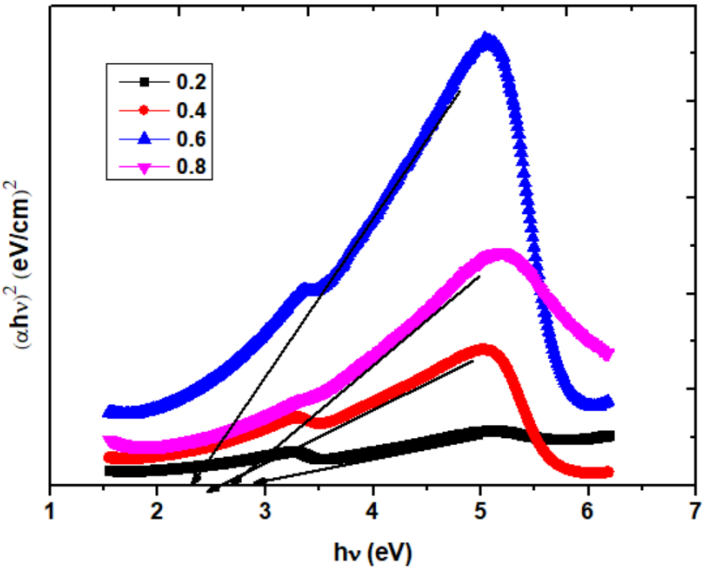

Figure 5. Tauc's plots of $Bi_{1-x}Ni_xFeO_3$ nanoparticles.

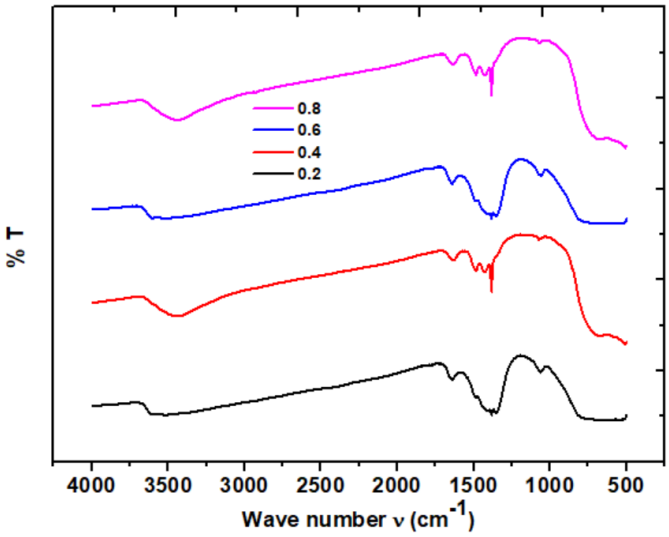

Figure 6. FTIR spectra of $Bi_{1-x}Ni_xFeO_3$ (x = 0.20–0.80) nanoparticles.

Table 2. FTIR spectral peak positions of $Bi_{1-x}Ni_xFeO_3$ (x = 0.20–0.80) nanoparticles.

x	Wavenumber of vibration bands (cm^{-1})
0.2	769.23, 1055.3, 1380.6, 1651.4, 3595.3
0.4	706.7, 1063.3, 1380.6, 1435.1, 1473.5, 1620.9, 3440.71
0.6	815.7, 1055.3, 1372.6, 1481.6, 1636.2, 3595.4
0.8	691.5, 1070.5, 1388.6, 1411.9, 1488.7, 1628.2, 3424.7

The electronic properties of BNFO nanoparticles are studied by evaluating dielectric constant (ε'), dielectric loss (ε''), ac-electrical conductivity ($\sigma_{ac} = \varepsilon_o\varepsilon''\omega$), dielectric modulus (M') and imaginary part of dielectric modulus (M'') as a function of log ω at room temperature. Figure 7 shows the plots between ε'-log ω and ε''-log ω for BNFO nanoparticles. The dielectric constant versus frequency plots conveys the high magnitude of dielectric constant at low frequencies ranging between 100 and 1 kHz. This kind of manner can be ascribed due to the grain boundary effect having high resistivity at this moment i.e., according to double layer theory/Koop's theory [57]. This induces the formation of several dipoles at the boundary leading to high polarization. Subsequently, the dielectric constant as well as dielectric loss get increased. This is elucidated by Maxwell and Wagner, and hence this polarization was known as Maxwell-Wagner interfacial polarization [58,59]. Similar kinds of mechanisms are discussed by Hiti [60], in the case of spinel ferrites. As we go for higher input field frequencies, the dielectric dispersion takes place. Then, the accumulation of charge carriers gets disturbed, and hence, it leads to a decrease of polarization and mostly prefers to the development of electrical conductivity. A similar approach is noted in the literature [61–63]. The plots reflect the fluctuated kind of data points. It can be attributed to the existence of little moisture, defects etc., in the BNFO samples as reported in the literature [64–66]. Figure 8 depicts the log ac-electrical conductivity versus log ω for which even the power law fit is done. This fitting provides the information related to the frequency dependent conductivity term pertaining to the two terms as frequency dependent, and frequency independent like this: $\sigma_{ac}(\omega, T) = \sigma_{dc}(T) + A\omega^n(\omega)$, wherein, the $\sigma_{dc}(T)$ is frequency independent or temperature dependent term and $A\omega^n(\omega)$ is the frequency dependent/temperature independent term [67–69]. The temperature dependent conductivity indicates the dc-conductivity values of x = 0.20–0.80 as listed in Table 3. Likewise, the frequency dependent term is the ac-conductivity value having the exponent '*n*' value. Usually, the exponent must be less than unity. This discloses the ratio of back hop rate to that of the site relaxation rate. That is, in the case of the exponent less than the unity, the frequency-dispersive AC-conductivity due to hopping the M'-log ω and M''-log ω plots (Figure 9) Z' versus Z'' plots (Figure 10) are incomplete relaxation in nature. This establishes the fact that the carriers have weak relaxation strength and move for longer distances [70–72]. The perovskite materials with different electrical, sensing and other properties are investigated and they are in comparison with literature [70–73]. If the assumed arc is provided to the Z' versus Z'' plots (Figure 10), the center of the arc lies below the real axis which justifies the presence of non-Debye relaxation as shown in the literature [73].

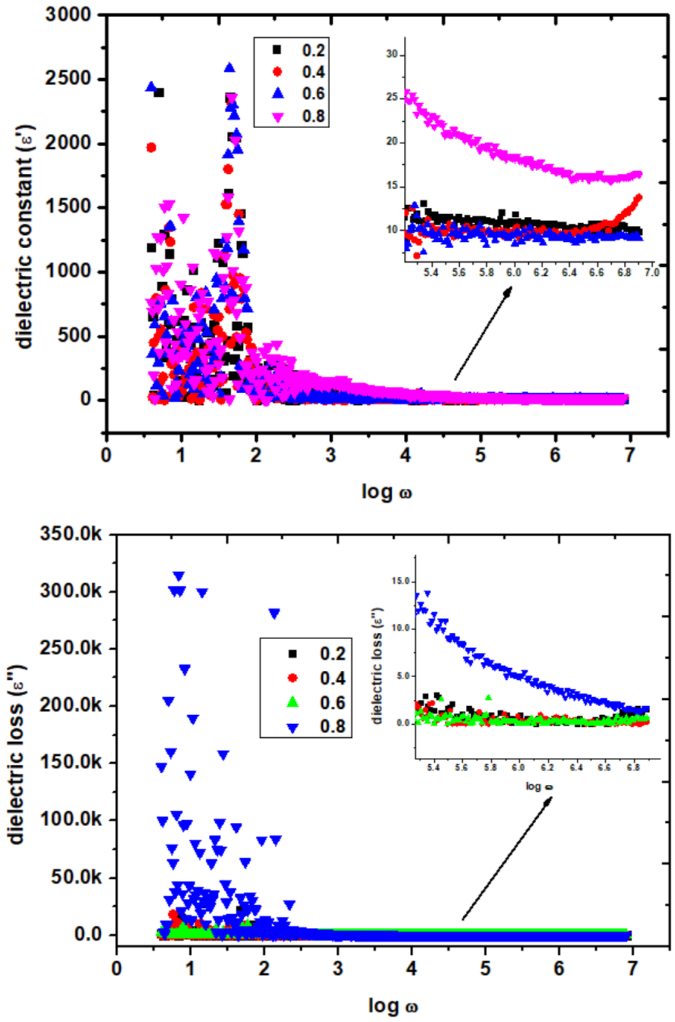

Figure 7. Frequency variation of dielectric constant and loss for $Bi_{1-x}Ni_xFeO_3$ (x = 0.20–0.80) nanoparticles.

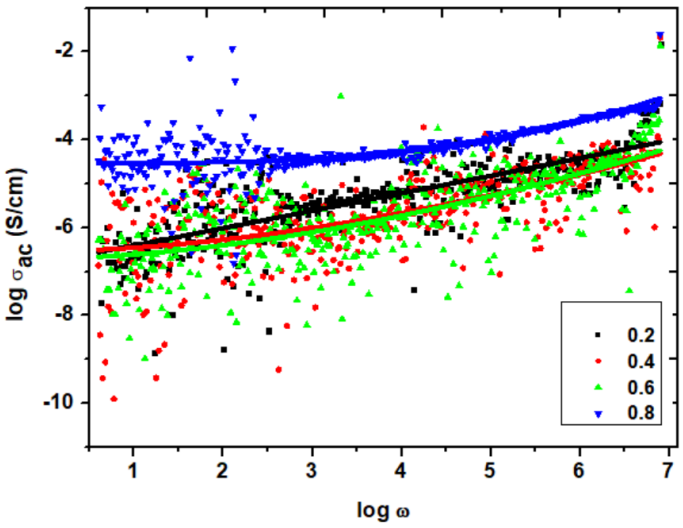

Figure 8. Frequency dependence of ac-electrical conductivity and power law fit for $Bi_{1-x}Ni_xFeO_3$ (x = 0.20–0.80) nanoparticles.

Table 3. Dielectric, conductivity and impedance of BNFO nanoparticles.

x	f (MHz)	ε'	ε"	logσac	M'	M"	Z' (Ω)	Z" (Ω)
	6	10.2	1.3	−3.3961	0.09686	0.01231	458.413	−3982.40
0.2	7	10.0	1.2	−3.1953	0.09533	0.01597	419.664	−3498.83
	8	9.9	1.57	−3.1694	0.09658	0.01499	410.642	−3018.01
	6	11.2	0.15	−4.3436	0.08958	0.00117	15.6327	−3727.52
0.4	7	12.5	0.003	−4.6550	0.08293	4.08×10^{-4}	51.3848	−2801.45
	8	13.8	0.23	−3.9995	0.07385	0.00127	22.3674	−2417.70
	6	9.4	0.66	−3.6851	0.10584	0.00748	211.373	−4518.92
0.6	7	9.2	0.57	−3.4250	0.10709	0.01169	339.008	−3829.19
	8	9.1	0.66	−3.5485	0.10453	0.0072	177.238	−3398.50
	6	16.0	1.56	−3.3147	0.06206	0.00606	247.661	−2617.04
0.8	7	16.2	1.34	−3.2833	0.06183	0.00538	193.726	−2140.77
	8	16.4	1.66	−3.1444	0.06006	0.00606	157.905	−1887.26

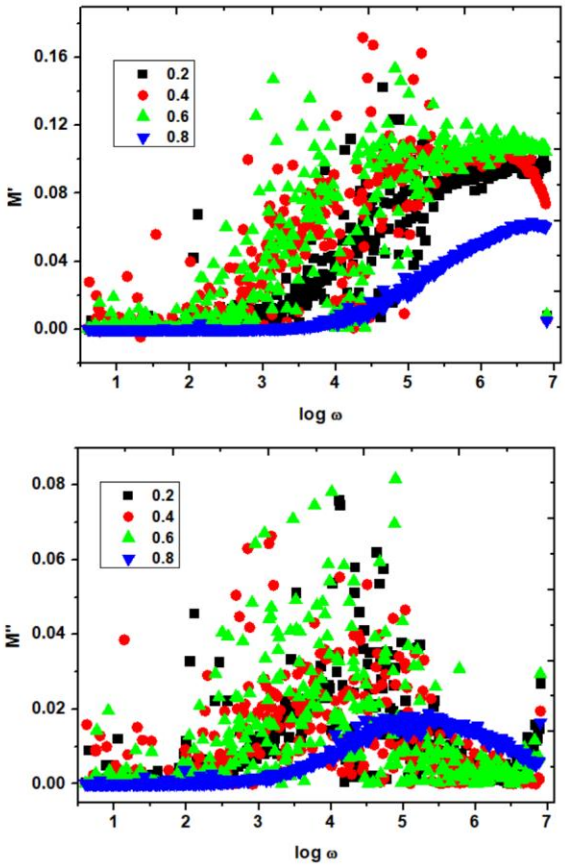

Figure 9. Frequency variation of real and imaginary parts of complex dielectric modulus for $Bi_{1-x}Ni_xFeO_3$ (x = 0.20–0.80) nanoparticles.

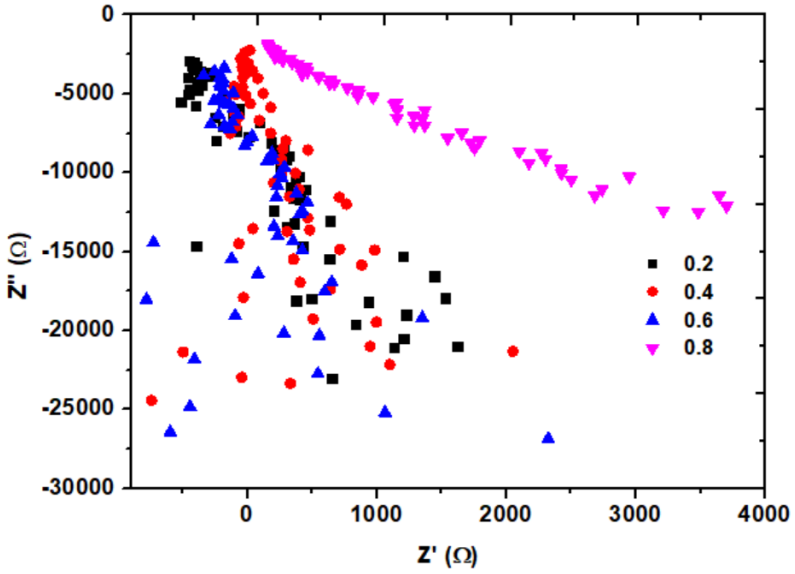

Figure 10. Cole-Cole (Nyquist) plots of $Bi_{1-x}Ni_xFeO_3$ (x = 0.20–0.80) nanoparticles.

5. Conclusions

Low temperature hydrothermal process is used in order to synthesize the BNFO nanoparticles. The XRD analysis confirms the rhombohedral crystal structure with the high crystallinity pertaining to the (104), and (110) reflection planes of BF, and the secondary phases are related to the $Bi_2Fe_4O_9$. The lattice constants are found to be enhanced from 5.571–5.581 Å (a = b), and 13.875–13.882 Å (c) as a function of Ni-content. Besides, the X-ray density is decreasing from 8.932 to 5.697 g/c.c., with 'x'. The examination of microstructure confirms that the average grain size varies between 129.3 and 186.8 nm. This manner is not monotonic and can be attributed to the strain formed during the reaction process to form final compounds. The TEM shows the existence of BNFO nanoparticles, and the SAED patterns support the formed XRD patterns having concentric circular rings like intense spots. The bandgap E_g values decreased from x = 0.2–0.6 from 2.928–2.334 eV while by x = 0.8, it increased to 2.723 eV. However, the bandgap range is wide, and hence the optoelectronic applications can be expected with the BNFO samples. The bands formed between 400 and 500 cm^{-1} are due to metal oxide bonds like Bi-O, Ni-O and Fe-O. The bands formed at 691.5–815.7 cm^{-1} can be attributed to the formation of secondary phase structures in the BNFO perovskite system. The x = 0.4 reveals the high dielectric constant (11.2–13.8), and low dielectric loss (0.003–0.23). On the other hand, x = 0.8 shows the high dielectric constant (16–16.4), and high dielectric loss (1.34–1.66) at 6, 7 and 8 MHz frequencies. These results at high frequencies confirmed that the x = 0.4 sample may be considered for charge stored capacitor applications while the x = 0.6 offers the dielectric absorber applications. Further, the log σ_{dc} values are found to be −6.786, −6.539, −6.707 and −4.538 for x = 0.20–0.80, respectively.

Acknowledgments: The author D. Baba Basha extends the appreciation to the Deanship of Postgraduate Studies and Scientific Research at Majmaah University for funding this research work through the project number (R-2026-33).

Availability of Data and Materials: The datasets used and analyzed during the current study are available from the corresponding author on reasonable request.

Funding: This research was funded by [Deanship of Postgraduate Studies and Scientific Research at Majmaah University] grant number [R-2026-33].

Author Contributions: Conceptualization, SD; methodology, SD; software, SD; validation, LSSR and DBB; formal analysis, SD; investigation, SD; resources, LSSR; data curation, MC; writing—original draft preparation,

MC; writing—review and editing, MC; visualization, DBB; supervision, LSSR; project administration, DBB; funding acquisition, DBB. All authors have read and agreed to the published version of the manuscript. All authors contributed to editorial changes in the manuscript. All authors fully participated in this research and agree to take responsibility for all aspects of this work.

Conflicts of Interest: The authors declare that they have no conflicts of interest.

References

1. Mitzi, D.B. Introduction: Perovskites. *Chemical Reviews* 2019, 119(5), 3033–3035. https://doi.org/10.1021/acs.chemrev.8b00800
2. Liu, H.; Yang, X. A brief review on perovskite multiferroics. *Ferroelectrics* 2017, 507(1), 69–85. https://doi.org/10.1080/00150193.2017.1283171
3. Korde, V.B.; Khot, S.; Kamble, D.B.; et al. Review: Perovskite nanostructures materials versatile platform for advance biosensor applications. *Sensors and Actuators Reports* 2024, 7, 100201. https://doi.org/10.1016/j.snr.2024.100201
4. Yin, Y.; Li, Q. A review on all-perovskite multiferroic tunnel junctions. *Journal of Materiomics*. 2017, 3(4), 245–254. https://doi.org/10.1016/j.jmat.2017.09.001
5. Suresh, K. N.; Chandra, B.N.K. A review on perovskite solar cells (PSCs), materials and applications. *Journal of Materiomics* 2021, 7(5), 940–956. https://doi.org/10.1016/j.jmat.2021.04.002
6. Mujtaba, A.; Khan, M.I.; Nadeem, M.A.; et al. Green hydrothermal synthesis of Mg-doped transition metal dichalcogenides using *Camellia sinensis* extract for enhanced energy storage. *Journal of Sol-Gel Science and Technology* 2025, 115, 457–470. https://doi.org/10.1007/s10971-025-06818-1
7. Verma, K.C.; Kotnala, R.K.; Goyal, N. Multiferroic Systems of BiFeO3 and BaTiO3 Nanostructures: New Ideas and Insights from Recent Magnetoelectric Advancements In: Nanostructured Multiferroics. Wiley; 2012. pp. 95–132. https://doi.org/10.1002/9783527809967.ch5
8. Visakh, P.M. Preparations, Characterization, and Applications of Multiferroic Nanocomposites. In: Nanostructured Multiferroics. Wiley; 2012. pp. 233–247. https://doi.org/10.1002/9783527809967.ch9
9. Carranza-Celis, D.; Cardona-Rodríguez, A.; Narváez, J.; et al. Control of Multiferroic properties in $BiFeO_3$ nanoparticles. *Scientific Reports* 2019, 9, 3182. https://doi.org/10.1038/s41598-019-39517-3
10. Indriyani, A.; Yulizar, Y.; Tri, Y.R.; et al. One-pot green fabrication of $BiFeO_3$ nanoparticles via *Abelmoschus esculentus* L. leaves extracts for photocatalytic dye degradation. *Applied Surface Science* 2021, 563, 150113. https://doi.org/10.1016/j.apsusc.2021.150113
11. Amdouni, W.; Fricaudet, M.; Otoničar, M.; et al. $BiFeO_3$ Nanoparticles: The "Holy-Grail" of Piezo-Photocatalysts? *Advanced Materials* 2023, 35(31), 2301841. https://doi.org/10.1002/adma.202301841
12. Parvathy, N.S.; Govindaraj, R. Atomic scale insights on the growth of $BiFeO_3$ nanoparticles. *Scientific Reports* 2022, 12, 4758. https://doi.org/10.1038/s41598-022-08687-y
13. Parida, S.; Nanda, J.; Sarangi, B.; et al. Plant extract mediated synthesis of $BiFeO_3$ nanoparticles for photocatalytic degradation of methylene blue dye. *Biomass Conversion and Biorefinery* 2025, 15, 11607–11622. https://doi.org/10.1007/s13399-024-06100-4
14. Basith, M.A.; Yesmin, N.; Hossain, R. Low temperature synthesis of $BiFeO_3$ nanoparticles with enhanced magnetization and promising photocatalytic performance in dye degradation and hydrogen evolution. *RSC Advances* 2018, 8(52), 29613–29627. https://doi.org/10.1039/c8ra04599b
15. Bai, X.; Bugnet, M.; Frontera, C.; et al. Crystal Growth Mechanisms of $BiFeO_3$ Nanoparticles. *Inorganic Chemistry* 2019, 58(17), 11364–11371. https://doi.org/10.1021/acs.inorgchem.9b00461
16. Cheng, Z.; Zhu, H.; Ji, H.; et al. Perovskite-Structured $BiFeO_3$ Nanoparticles with Abundant Oxygen Vacancies for Selective *n*-Butanol Gas Sensing. *ACS Applied Nano Materials* 2023, 6(24), 23370–23380. https://doi.org/10.1021/acsanm.3c04754
17. Wu, J.; Jin, X.; Wang, J.; et al. Enhancement of Photocatalytic Activity in $BiFeO_3$ Nanoparticles through Electrical Polarization. *Advanced Energy and Sustainability Research* 2025, 6(7), 2400285. https://doi.org/10.1002/aesr.202400285
18. Wu, J.; Mao, W.; Wu, Z.; et al. Strong pyro-catalysis of pyroelectric $BiFeO_3$ nanoparticles under a room-temperature cold–hot alternation. *Nanoscale* 2016, 8(13), 7343–7350. https://doi.org/10.1039/c6nr00972g
19. Mocherla, P.S.V.; Karthik, C.; Ubic, R.; et al. Tunable bandgap in $BiFeO_3$ nanoparticles: The role of microstrain and oxygen defects. *Applied Physics Letters* 2013, 103(2), 022910. https://doi.org/10.1063/1.4813539

20. Prince, M.H.; Aishi, T.M.; Zubair, Md. A.; et al. Tuning of the Structural, Optical and Magnetic Properties of BiFeO3 Nanoparticles by Annealing. In: *Tuning of the Structural, Optical and Magnetic Properties of BiFeO3 Nanoparticles by Annealing*, Proceedings of the 2023 IEEE International Conference on Telecommunications and Photonics (ICTP); 21–23 December 2023, Dhaka, Bangladesh. IEEE; 2023, pp. 01–05. https://doi.org/10.1109/ictp60248.2023.10490725
21. Masoudpanah, S.M.; Mirkazemi, S.M. *Journal of Nanostructures* 2017, 7(3), 183–188. https://doi.org/10.22052/jns.2017.03.003
22. Othman, M.; Mallek-Zouari, I.; Akrout, H.; et al. Synthesis and properties of ultra-small $BiFeO_3$ nanoparticles doped with cobalt. *Ceramics International* 2023, 49(7), 10580–10587. https://doi.org/10.1016/j.ceramint.2022.11.245
23. Haider, S.; Liaquat, A.; Awan, M.S.; et al. Electrical and magnetic properties of $BiFeO_3$ nanoparticles substituted with high concentrations of cobalt. *Journal of the Australian Ceramic Society* 2021, 57, 643–650. https://doi.org/10.1007/s41779-021-00560-x
24. Papadopoulos, K.; Myrovali, E.; Dubey, A.; et al. Control of physical properties in $BiFeO_3$ nanoparticles via Sm^{3+} and Co^{2+} ion doping. *Nanotechnology* 2023, 35(1), 015707. https://doi.org/10.1088/1361-6528/acfcc2
25. Shrimali, V.G.; Rathod, K.N.; Dhruv, D.; et al. Magnetoelectric properties of Co-doped $BiFeO_3$ nanoparticles. *International Journal of Modern Physics B* 2018, 32(12), 1850143. https://doi.org/10.1142/s0217979218501436
26. Gu, Y.; Huang, N.; Guo, C.; et al. Sm-Eu Co-Doped $BiFeO_3$ Nanoparticles With Superabsorption and Electrochemical Oxygen Evolution Reaction. *Frontiers in Physics* 2022, 10, 1–8. https://doi.org/10.3389/fphy.2022.853179
27. Apostolova, I.; Apostolov, A.; Wesselinowa, J. Magnetoelectric Coupling Effects in Tb-Doped $BiFeO_3$ Nanoparticles. *Magnetochemistry* 2023, 9(6), 142. https://doi.org/10.3390/magnetochemistry9060142
28. Gu, Y.; Zhou, Y.; Zhang, W.; et al. Optical and magnetic properties of Sm-doped $BiFeO_3$ nanoparticles around the morphotropic phase boundary region. *AIP Advances* 2021, 11(4), 045223. https://doi.org/10.1063/5.0042485
29. Haruna, A.; Abdulkadir, I.; Idris, S.O. Photocatalytic activity and doping effects of $BiFeO_3$ nanoparticles in model organic dyes. *Heliyon* 2020, 6(1), e03237. https://doi.org/10.1016/j.heliyon.2020.e03237
30. Wang, Y.-H.; Qi, X. The Effects of Nickel Substitution on Bismuth Ferrite. *Procedia Engineering* 2012, 36, 455–461. https://doi.org/10.1016/j.proeng.2012.03.066
31. Mishra, D.K.; Qi, X. Energy levels and photoluminescence properties of nickel-doped bismuth ferrite. *Journal of Alloys and Compounds* 2010, 504(1), 27–31. https://doi.org/10.1016/j.jallcom.2010.05.107
32. Nadeem, M.; Khan, W.; Khan, S.; et al. Significant enhancement in photocatalytic performance of Ni doped $BiFeO_3$ nanoparticles. *Materials Research Express* 2018, 5(6), 065506. https://doi.org/10.1088/2053-1591/aac70d
33. Nadeem, M.; Khan, W.; Khan, S.; et al. Temperature dependent dielectric response and conduction mechanism of nickel doped bismuth ferrite nanoparticles. In: *DAE SOLID STATE PHYSICS SYMPOSIUM 2018*, Proceedings of the DAE SOLID STATE PHYSICS SYMPOSIUM 2018; 18–22 December 2018; Hisar, Haryana, India. AIP Publishing; 2019. Volume 2115, p. 030098. https://doi.org/10.1063/1.5112937
34. Betancourt-Cantera, L.G.; Bolarín-Miró, A.M.; Cortés-Escobedo, C.A.; et al. Structural transitions and multiferroic properties of high Ni-doped $BiFeO_3$. *Journal of Magnetism and Magnetic Materials* 2018, 456, 381–389. https://doi.org/10.1016/j.jmmm.2018.02.065
35. Shameem, B.I.B.; Divya, L.S.; Kossar, S.; et al. Substitution driven optical and magnetic properties of neodymium and nickel doped BiFeO3 ceramics for spintronics applications. In Proceedings of the 2018 International Conference on Recent Trends in Electrical, Control and Communication (RTECC); 20–22 March 2018; Malaysia, Malaysia. pp. 93–98. https://doi.org/10.1109/rtecc.2018.8625635
36. Sarkar, K.; Mukherjee, S.; Mukherjee, S. Structural, electrical and magnetic behaviour of undoped and nickel doped nanocrystalline bismuth ferrite by solution combustion route. *Processing and Application of Ceramics* 2015, 9(1), 53–60. https://doi.org/10.2298/pac1501053s
37. Mukherjee, S.; Sarkar, K.; Mukherjee, S. Effect of Nickel and Cobalt Doping on Nano Bismuth Ferrite Prepared by the Chemical Route. *Interceram-International Ceramic Review* 2015, 64, 38–43. https://doi.org/10.1007/BF03401099
38. Ponraj, C.; Vinitha, G.; Daniel, J. Photocatalytic degradation of acid red-85 dye by nickel substituted bismuth ferrite nanoparticles. *Materials Research Express* 2019, 6(8), 084006. https://doi.org/10.1088/2053-1591/ab225f

39. Preethi, A.J.; Ragam, M. Effect of doping in multiferroic BFO: A review. *Journal of Advanced Dielectrics* 2021, 11(06), 2130001. https://doi.org/10.1142/s2010135x21300012
40. Routray, K.L.; Sanyal, D.; Behera, D. Gamma irradiation induced structural, electrical, magnetic and ferroelectric transformation in bismuth doped nanosized cobalt ferrite for various applications. *Materials Research Bulletin* 2019, 110, 126–134. https://doi.org/10.1016/j.materresbull.2018.10.019
41. Mallikarjuna, A.; Ramesh, S.; Suresh, K.N.; et al. Structural transformation and high negative dielectric constant behavior in (1-x) ($Al_{0.2}La_{0.8}TiO_3$) + (x) ($BiFeO_3$) (x = 0.2–0.8) nanocomposites. *Physica E: Low-dimensional Systems and Nanostructures* 2020,122, 114204. https://doi.org/10.1016/j.physe.2020.114204
42. Venkata, S.R.B.; Srinivas, K.; Suresh K.N.; et al. Nanorods like microstructure, photocatalytic activity and ac-electrical properties of (1-x) ($Al_{0.2}La_{0.8}TiO_3$) + (x) ($BaTiO_3$) (x = 0.2, 0.4, 0.6 & 0.8) nanocomposites. *Chemical Physics Letters* 2020, 752, 137552. https://doi.org/10.1016/j.cplett.2020.137552
43. Sahu, S.; Mohapatra, P.P.; Karnajit Singh, H.; et al. Enhanced microwave absorbing performance of Sr^{2+} substituted Nickel-Cobalt nano ferrite for radar and stealth applications. *Materials Science and Engineering: B* 2023, 294, 116514. https://doi.org/10.1016/j.mseb.2023.116514
44. Shannon, R.D. Revised effective ionic radii and systematic studies of interatomic distances in halides and chalcogenides. *Acta Crystallographica Section A* 1976, 32, 751–767. https://doi.org/10.1107/s0567739476001551
45. Scherrer, P. Bestimmung der Größe und der inneren Struktur von Kolloidteilchen mittels Röntgenstrahlen. *Nachrichten von der Gesellschaft der Wissenschaften zu Göttingen, Mathematisch-Physikalische Klasse* 1918, 1918, 98–100.
46. Kumar, N.S.; Suvarna, R.P.; Naidu, K.C.B. Sol-gel synthesized and microwave heated $Pb_{0.8-y}La_yCo_{0.2}TiO_3$ (y = 0.2–0.8) nanoparticles: Structural, morphological and dielectric properties. *Ceramics International* 2018, 44(15), 18189–18199. https://doi.org/10.1016/j.ceramint.2018.07.027
47. Mallikarjuna, A.; Ramesh, S.; Kumar, N.S.; et al. Structural transformation and high negative dielectric constant behavior in (1-x) ($Al_{0.2}La_{0.8}TiO_3$) + (x) ($BiFeO_3$) (x = 0.2–0.8) nanocomposites. *Physica E: Low-Dimensional Systems and Nanostructures* 2020, 122, 114204. https://doi.org/10.1016/j.physe.2020.114204
48. Dastagiri, S.; Lakshmaiah, M.V.; Chandra, B.N.K. Defect dipole polarization mechanism in low-dimensional europium substituted $Al_{0.8}La_{0.2}TiO_3$ nanostructures. *Physica E: Low-dimensional Systems and Nanostructures* 2020, 120, 114058. https://doi.org/10.1016/j.physe.2020.114058
49. Naidu, K.C.B.; Kumar, N.S.; Banerjee, P.; et al. A review on the origin of nanofibers/nanorods structures and applications. *Journal of Materials Science: Materials in Medicine* 2021, 32, 68. https://doi.org/10.1007/s10856-021-06541-7
50. Kadiyala, C.B.N.; Wuppulluri, M. Effect of microwave heat treatment on pure phase formation of hydrothermal synthesized nano NiMg ferrites. *Phase Transitions* 2017, 90(9), 847–862. https://doi.org/10.1080/01411594.2016.1277220
51. Lu, L.; Li, J.; Yu, J.; et al. A hierarchically porous $MgFe_2O_4/\gamma$-Fe_2O_3 magnetic microspheres for efficient removals of dye and pharmaceutical from water. *Chemical Engineering Journal* 2016, 283, 524–534. https://doi.org/10.1016/j.cej.2015.07.081
52. Yellanna, M.; Naidu, K.C.B.; Suresh, K.N.; et al. Magneto-dielectric and thermal study of Gd-doped nano nickelates. *Journal of Materials Science: Materials in Electronics* 2023, 34, 2307. https://doi.org/10.1007/s10854-023-11741-8
53. Machakanti, Y. Low-temperature hydrothermal synthesis of $NiEuFe_2O_4$ nanoparticles: Magnetic, thermal, and magneto-dielectric behavior. *International Journal of Applied Ceramic Technology* 2024, 21, 715–726. https://doi.org/10.1111/ijac.14574
54. Vidya, S.T.; Subba, R.T.; Naidu, K.C.B. Effect of calcination temperature on optical, magnetic and dielectric properties of Sol-Gel synthesized Ni0.2Mg0.8-xZnxFe2O4 (x = 0.0–0.8). *Ceramic International* 2020, 46(8), 11515–11529. https://doi.org/10.1016/j.ceramint.2020.01.178
55. Prakash, M.; Kumar, R.J.; C.B. Naidu, K. Optical and functional properties of hydrothermally synthesized tetragonal Ba0.4Cu0.6−xLaxTiO3 (x = 0.2–0.6) nanoparticles *Materials Research Express* 2020, 7(1), 015037. https://doi.org/10.1088/2053-1591/ab6494
56. Scott, J.F. Ferroelectrics go bananas. *Journal of Physics: Condensed Matter* 2008, 20, 021001. https://doi.org/10.1088/0953-8984/20/02/021001
57. Koops, C.G. On the Dispersion of Resistivity and Dielectric Constant of Some Semiconductors at Audiofrequencies. *Physical Review Journals* 1951, 83, 121–124. https://journals.aps.org/pr/abstract/10.1103/PhysRev.83.121

58. Maxwell, J.C. *A treatise on electricity and magnetism. Oxford: Clarendon Press.* 1873, Volume 2.
59. Wagner, W. The Distribution of Relaxation Times in Typical Dielectrics. *Annals of Physics* 1913, 40, 817. https://doi.org/10.1063/1.1745355
60. El Hiti, M.A. Dielectric behavior and ac electrical conductivity of Zn-substituted Ni Mg ferrites. *Journal of Magnetism and Magnetic Materials* 1996, 164, 187–196. https://doi.org/10.1016/s0304-8853(96)00368-x
61. Mallikarjuna, A.; Singampalli, R.; Nagasamudram, S.K.; et al. Crystal Research and Technology. Wiley; 2020. Volume 55, Issue 7. https://doi.org/10.1002/crat.202000068
62. Reddy, B.V.S.; Srinivas, K.; Kumar, N.S.; et al. Phase transformation, nanorod-like morphology, wide bandgap, and dielectric properties of $1-x$ ($Al_{0.2}La_{0.8}TiO_3$) + x ($BaTiO_3$) (x = 0.2–0.8) nanocomposites. *Journal of Materials Science: Materials in Electronics* 2020, 31, 9293–9305. https://doi.org/10.1007/s10854-020-03469-6
63. Kumar, N.S.; Suvarna, R.P.; Naidu, K.C.B. Multiferroic Nature of Microwave-Processed and Sol-Gel Synthesized Nano$Pb_{1-x}Co_xTiO_3$ (x = 0.2–0.8) Ceramics. *Crystal Research and Technology* 2018, 53(12), 1800139. https://doi.org/10.1002/crat.201800139
64. Mallikarjuna, A.; Kumar, N.S.; Babu, T.A.; et al. Structural and Dielectric Properties of (1-x) ($Al_{0.2}La_{0.8}TiO_3$) + (x) ($BiZnFeO_3$) (x = 0.2 – 0.8) nanocomposites. *Journal of Inorganic and Organometallic Polymers and Materials* 2021, 31, 4512–4522. https://doi.org/10.1007/s10904-021-02123-w
65. Rahman, M.T.; Ramana, C.V. *Journal of Applied Physics* 2014, 116, 164108-10.
66. Kumari, P.A.; Devi, D.M.; Kumar, N.S.V. Effect of pH on Structure, Optical, and Dielectric Properties of $BaTiO_3$ Nanoparticles. *Crystal Research and Technology* 2023, 58(8). https://doi.org/10.1002/crat.202300022
67. Reddy, V.S.B.; Srinivas, K.; Kumar, S.N.; et al. Nanorods like microstructure, photocatalytic activity and ac-electrical properties of (1-x) ($Al_{0.2}La_{0.8}TiO_3$) + (x) ($BaTiO_3$) (x = 0.2, 0.4, 0.6 & 0.8) nanocomposites. *Chemical Physics Letters* 2020, 752, 137552. https://doi.org/10.1016/j.cplett.2020.137552
68. Kumar, N.S.; Suvarna, R.P.; Naidu, K.C.B. Negative dielectric behavior in tetragonal $La_{0.8}Co_{0.2-x}Eu_xTiO_3$ (x = 0.01–0.04) nanorods. *Materials Characterization* 2020, 166, 110425. https://doi.org/10.1016/j.matchar.2020.110425
69. Naidu, K.C.B.; Kiran, S.R.; Madhuri, W. Investigations on transport, impedance and electromagnetic interference shielding properties of microwave processed NiMg ferrites. *Materials Research Bulletin* 2017, 89, 125–138. https://doi.org/10.1016/j.materresbull.2017.01.015
70. Bharathi, K.; Chandra, B.N.K.; Veena, E.; et al. AlxNi1−xTiO3+δ (x = 0.2–0.8) nanomaterials for dielectric absorber applications *Journal of Materials Science: Materials in Electronics* 2025, 36, 1522. https://doi.org/10.1007/s10854-025-15598-x
71. Baba, B.D.; Suresh, K.N.; Naidu, C.B.; et al. Structural, electrical, and magnetic properties of nano $Sr_{1-x}La_xFe_{12}O_{19}$ (X = 0.2–0.8). *Scientific Reports* 2022, 12, 12723. https://doi.org/10.1038/s41598-022-15250-2
72. Rajender, T.; Naidu, K.C.B. Magnetic, dielectric and thermal study of $CoNiFe_2O_4$ nanoparticles. *Nano-Structures & Nano-Objects* 2024, 38, 101167. https://doi.org/10.1016/j.nanoso.2024.101167
73. Tian, R.; Shi, X.; Song, P. MOFs-derived ZnO dodecahedrons decorated with perovskite $CsPbBr_3$ quantum dots for efficient detection of ethanolamine. *Sensors and Actuators B: Chemical* 2026, 447, 138856. https://doi.org/10.1016/j.snb.2025.138856